JMEPEG (2021) 30:8831–8840
https://doi.org/10.1007/s11665-021-06340-9

1059-9495/$19.00

Comparing Compression Deformation and Rate Sensitivity of Additively Manufactured and Extruded-Annealed 316L Alloys

Samed Enser, Hakan Yavas, Burcu Arslan Hamat, Hüseyin Aydın, Gülten Kafadar, A. Alptuğ Tanrıkulu, Havva Zeytin Kazdal, Fahrettin Ozturk, and Mustafa Güden

Submitted: 31 January 2021 / Revised: 14 September 2021 / Accepted: 25 September 2021 / Published online: 2 November 2021

The deformation behavior of a selective-laser-melt-processed 316-L alloy (SLM-316L) under compression was determined together with a commercial annealed-extruded 316L alloy bar (C-316L) for comparison. Strain rate jump tests and hardness tests on the untested and compression tested samples were also performed. Extensive microscopic observations on the deformed and undeformed samples showed a twinning-dominated deformation in SLM-316L, similar to twinning-induced-plasticity steels, while a martensitic transformation-dominated deformation in C-316L alloy, similar to transformation-induced-plasticity steels. Within the studied quasi-static strain rate regime, the measured higher strain rate sensitivity of SLM-316L was ascribed to the lower distances between the nano-twins, in the level of 100 nm, than the distances between martensite plates, in the level of 1000 nm. A higher hardness increase in the martensite transformation region as compared with the twinned region proved the higher work hardening of C-316L. The hardness tests in the micron and sub-micron levels further confirmed the previously determined relatively low resistances of the dislocation cell walls (sub-grain) to the dislocation motion in SLM-316L alloy.

Keywords 316L, additive manufacturing, compression, hardness, rate sensitivity

1. Introduction

Selective-laser-melt (SLM) metal additive manufacturing (AM) is a near-net-shape manufacturing technique, reducing the secondary processing steps (Ref 1). Extremely high (10^3-10^8 K/s) (Ref 2) cooling rates in SLM cause residual stresses (Ref 3-5), inhomogeneous microstructure, variable mechanical properties, and porosities (Ref 6-8). The SLM-processed 316-L alloy (SLM-316L), for example, develops a microstructure composed of columnar grains aligned through the laser building direction and sub-grains of micro/nano size inter-grain cells (cell structure) (Ref 9-18). A twinning-induced-plasticity (TWIP) of SLM-316L alloy was also previously reported (Ref 14,16,17,19). The measured yield strengths are higher than those of conventionally processed ones (Ref 16,20,21), and the anisotropy in the yield, flow stress, and ductility has also been reported; the yield and flow stress are higher in the normal to the building direction, and the ductility is vice versa (Ref 16,17). As twinning is an important deformation mechanism in SLM-316L at quasi-static strain rates, the response of the alloy to strain rates is to be identified. The effect of strain rate on the tensile flow stress of SLM-316L stainless steel was previously determined between 5×10^{-5} and 1×10^{-1} s^{-1} (Ref 22). The measured strain rate sensitivity of SLM-316L was reported much higher than that of coarse-grained 316L, with a smaller deformation activation volume. It was suggested that the plastic deformation rate-controlling scale of SLM-316L was three orders of magnitude smaller than the measured average grain size. Contrarily, the rate sensitivity of an SLM-316L alloy was reported smaller than that of a C-316L alloy under compression between quasi-static and high strain rates up to ~ 2000 s^{-1} (Ref 23).

The present study is a continuation of the above studies and focused on the compression flow stress and hardness behavior of an SLM-316L within the quasi-static strain rate range (10^{-4}-10^{-2} s^{-1}). The strain rate sensitivity was determined in the normal to the building direction, and strain rate jump tests were performed to clarify the existence of any strain rate effect. The strain rate sensitivity of a commercially available commercial extruded-annealed 316L bar (C-316L) was also determined for comparison within the same strain rate regime. Extensive microscopic studies were also performed on the deformed cross-sections of SLM-316L and C-316L samples tested at low strain rates to correlate the detected hardness, flow stress, and

This invited article is part of a special topical focus in the *Journal of Materials Engineering and Performance* on Additive Manufacturing. The issue was organized by Dr. William Frazier, Pilgrim Consulting, LLC; Mr. Rick Russell, NASA; Dr. Yan Lu, NIST; Dr. Brandon D. Ribic, America Makes; and Caroline Vail, NSWC Carderock.

Samed Enser and **Mustafa Güden**, Department of Mechanical Engineering, İzmir Institute of Technology, Urla, Izmir, Turkey; **Hakan Yavas, Burcu Arslan Hamat, Gülten Kafadar,** and **A. Alptuğ Tanrıkulu**, Additive Manufacturing Excellence Center, Turkish Aerospace Industries, Kahramankazan, Ankara, Turkey; **Hüseyin Aydın** and **Havva Zeytin Kazdal**, Division of Materials Science, TUBITAK-MAM, Gebze, Turkey; **Fahrettin Ozturk**, Additive Manufacturing Excellence Center, Turkish Aerospace Industries, Kahramankazan, Ankara, Turkey; and Department of Mechanical Engineering, Ankara Yıldırım Beyazıt University, Etlik, Ankara, Turkey. Contact e-mail: hakan.yavas@tai.com.tr.

strain rate sensitivity difference between the two alloys with deformation microstructure.

2. Materials, Processing, and Experimental Techniques

The test samples were fabricated in a laser powder bed fusion AM Concept Laser M2 Cushing device (400 W continuous-wave fiber laser) using gas atomized 316L powders with an average size of 10-45 μm under a nitrogen atmosphere. The power, scanning rate, hatching space, and spot size of the incident beam were, respectively, 370 W, 900 mm s^{-1}, 95 μm, and 160 μm. A multidirectional scanning (biaxial scanning) laser-pattern rotated 90° between adjacent layers and patented by the manufacturer was used to construct the samples with a constant layer thickness of 30 μm. The hardness and compression test samples were machined from a 6x13x130 mm rectangular bar fabricated in the z-direction or building direction (Fig. 1a). After removing the supports and machining the bar 0.5 mm from each side, the cylindrical compression test samples, 5 mm in diameter and 5 mm in length, were prepared using an electro-discharge machine (Fig. 1a). Quasi-static compression tests were performed in a Shimadzu AG-X Universal Test machine at 1×10^{-4}, 1×10^{-3}, and 1×10^{-2} s^{-1}, using a tool steel ring around the test samples to compress the samples until about various prescribed strains. The compression tests were performed on the *x*-axis (the *yz*-plane, parallel to the biaxial plane, Fig. 1b and c). The strain was calculated both from the machine compliance corrected stroke and the video extensometer displacement (placed on the edge of the compression test plate). A total of three tests were performed at each quasi-static strain rate. For comparison, the compression tests (5 mm in diameter and 5 mm in length) and Vickers Hardness tests were also prepared on C-316L alloy. The loading axis was the extrusion direction (ED). The chemical composition of the alloy is tabulated in Table 1, and the average grain size was determined $\sim$ 40 μm by the linear intercept method.

Nano-indentation tests were performed in the *yz*- and *xy*-planes using a Bruker Hysitron TI 980 (Bruker MA, US) and CSM Instruments NHTTX 01-03089 (Anton Paar, DE) equipped with a Berkovich tip (tip radius is approximately 25 nm for both nano-indenters). The calibration was performed in accordance with the methods described by Oliver and Pharr (Ref 24,25). The machine compliance calibration was made by calculating the slope of load vs. stiffness as a function of indenter displacement. The nano-hardness was made normal to the *yz*-plane (parallel to the *x*-axis, through melt pools) (Fig. 1b) and the *xz*-plane (parallel to the *z*-direction) (Fig. 1c). Vickers Hardness tests were performed on the polished and polished-etched surfaces of mounted samples in a Shimadzu Micro Vickers Hardness Tester by applying the loads at 0.49, 0.98, 1.96, 2.94, 4.9, 9.81, and 19.61 N for 10 ms. X-ray diffraction (XRD) was used to determine the crystallographic structure and phase quantification of SLM-316L and C-316L untested and compression tested samples. XRD analysis was performed on a Philips X'Pert Pro x-ray diffraction device using CuKα radiation (λ = 1.54 Å) at 40 kV. The XRD analysis was carried

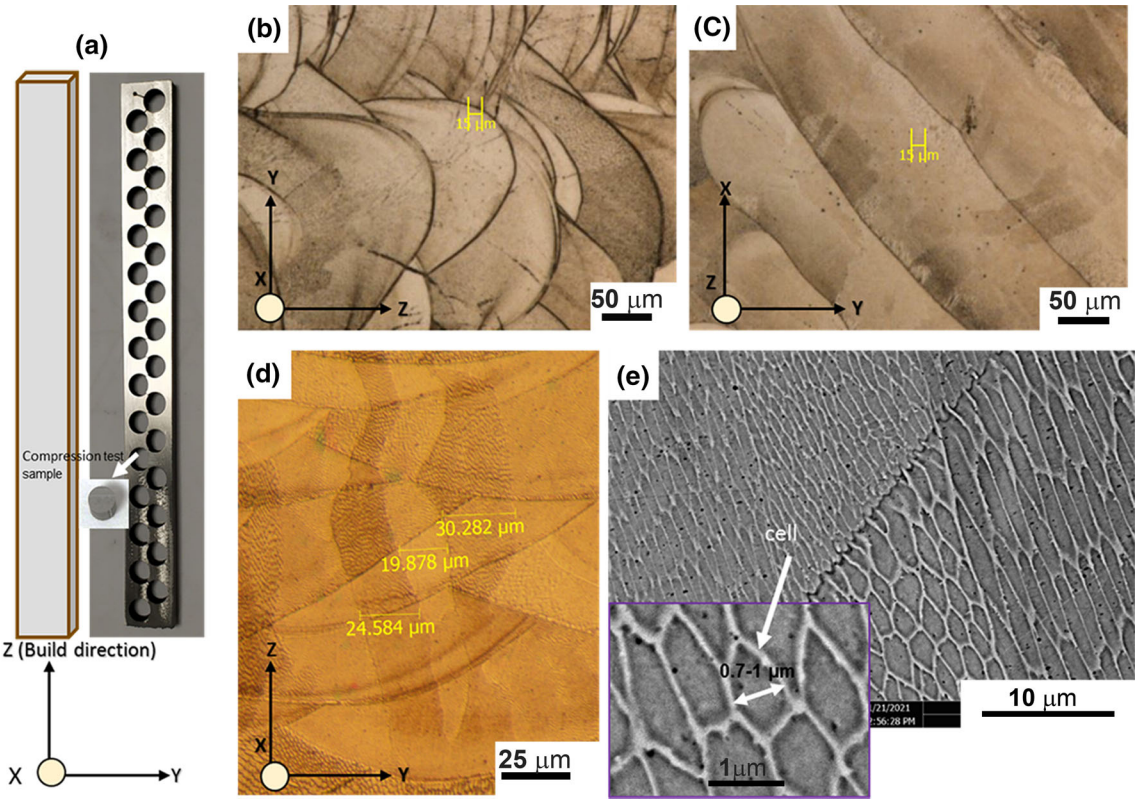

Fig. 1 (a) SLM-316L bar sample and the optical micrographs of nano hardness tests through (b) *yz*-plane (parallel to the *x*-direction) and (c) *xz*-plane (parallel to the *z*-direction), (d) optical micrograph showing the columnar grains in the *yz*-plane and (e) the cell structure within the grains

Table 1 Chemical composition of C316-L (Viraj Impoexpo)

C	Mn	Si	S	P	Ni	Cr	Mo	Cu	N	Co	Fe
0.022	1.40	0.45	0.021	0.034	10.04	16.30	2.05	0.38	0.069	0.19	Bal.

from 40° to 150° intervals at a $0.02°s^{-1}$ scanning rate. The weight percentage of the martensite in C-316L specimens was determined by the Rietveld profile refinement method (Ref 26) using a High Score X'pert program. This method is based on monitored intensities in an XRD pattern. A least-squares approach is used to refine a theoretical background profile until it matches the measured pattern profile. The integrated intensities of individual peaks for each phase in the alloy or mixture are determined to calculate weight percentages.

The density of SLM-316L specimens was determined by the Archimedes method as

$$\rho = \frac{w_{\text{air}}\ \rho_{\text{water}}}{w_{\text{air}} - w_{\text{water}}} \quad \text{(Eq 1)}$$

where w is the weight and ρ is the density. The percent porosity ($\%P$) was calculated as

$$\%P = 100\left(1 - \frac{\rho}{\rho_b}\right) \quad \text{(Eq 2)}$$

where ρ_b is the density of bulk 316L alloy, which was determined by measuring the density of C-316L alloy using the same Archimedes method. The metallographic samples were etched using an etching solution composing of 10% HNO_3, 20% HCl and 20% Glycerol. The microscopic analysis was performed in a Meiji IM7 100 optical microscope and an FEI Quanta 205 FEG and Philips XL 30SFEG scanning electron microscope (SEM).

3. Results and Discussion

3.1 Density and Microstructural Characterization

The average densities of SLM-316L and C-316L were, respectively, 7821 ± 5 kg m^{-3} and 7838.5±5 kg m^{-3} determined by the Archimedes method. The percent porosity in SLM-316L was 0.22, comparable with the reported density using the similar processing parameters (Ref 22). The XRD spectra of the untested samples of SLM-316L and C-316L shown in Fig. 2 furthermore confirm a fully austenitic phase (γ) in both alloys, while the compression tested (51% strain) C-316L sample exhibits martensite phase ($\alpha'(110)$ and $\alpha'(211)$ peaks in Fig. 2). The martensite content of the undeformed and deformed C-316L samples was calculated using the $\alpha'(110)$ and $\gamma(111)$ peaks in Fig. 2.

The microstructure of SLM-316L in the yz-plane is composed of columnar grains, as seen in Fig. 1(d). The width of these grains is 20-50 μm, and the lengths are several times the melt pool size. A crystallographic fiber texture formation is usually reported for SLM-316L: <100> directions are aligned in the building direction (z-axis) (Ref 17,27-31). Rotation scanning, however, causes a mismatch in the positions of melt layers, leading to overlapping semi-ellipse melt pools rather than nail-top appearance and interrupted columnar grains, as

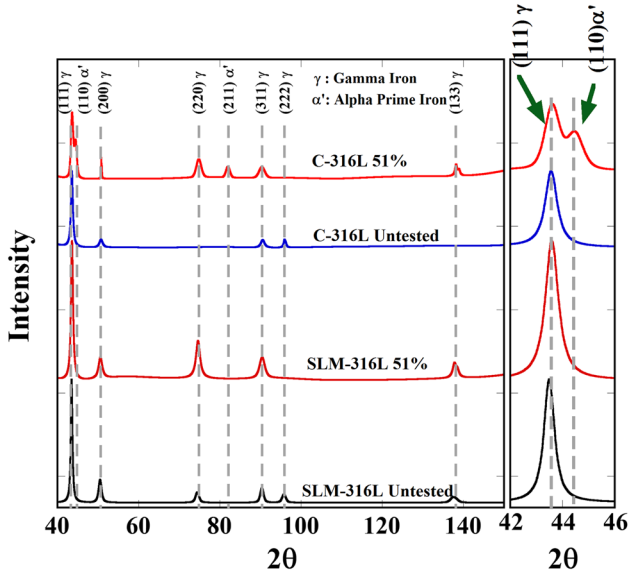

Fig. 2 XRD spectra of untested and compression tested (51% strain) SLM-316L and C-316L samples

seen in Fig. 1(d). Furthermore, rotation scanning results in a strong <110> fiber texture along the building direction and random orientations of the directions normal to the building direction (Ref 32). A well-known cellular microstructure/sub-structure (sub-grain) development in the grains is also seen in Fig. 1(e). The lengths of the cellular structure may be up to several times the melt pool size as with columnar grains, and the widths range 0.7-1 μm (shown in the inset of Fig. 1e). The microstructure of SLM-316L in the yz-plane consists of biaxial (± 45°) melt pools, as seen in Fig. 1(c). The grain development during laser melting and solidification in xz-plane is different from the parallel to the building direction and is mostly composed of equal-axed grains with the sizes of 20-50 μm. Similarly, a cellular microstructure/sub-structure development was also seen in this plane.

3.2 Compression Tests and Strain Rate Sensitivity

The compression true stress-strain curves of SLM-316L and C-316L at 10^{-3} s^{-1} are shown in Fig. 3(a) until about 0.5 true strain, together with the representative work hardening (WH) curves for each alloy. SLM-316L has a higher average yield strength (proof strength), 510 ± 10.2 MPa (12 tests), than C316L, 360 ± 11.6 MPa. Since both alloys have broadly similar grain sizes (excluding sub-grains in SLM-316L), the higher yield strength of SLM-316L is ascribed to the higher dislocation density of SLM-316L (Ref 16). The dislocation density for an SLM-316L alloy was previously reported as $\sim 1.14 \times 10^{15}$ m^{-2} (Ref 16), and taking the average dislocation density of C316-L alloy 3.8×10^{14} m^{-2} (Ref 33), the

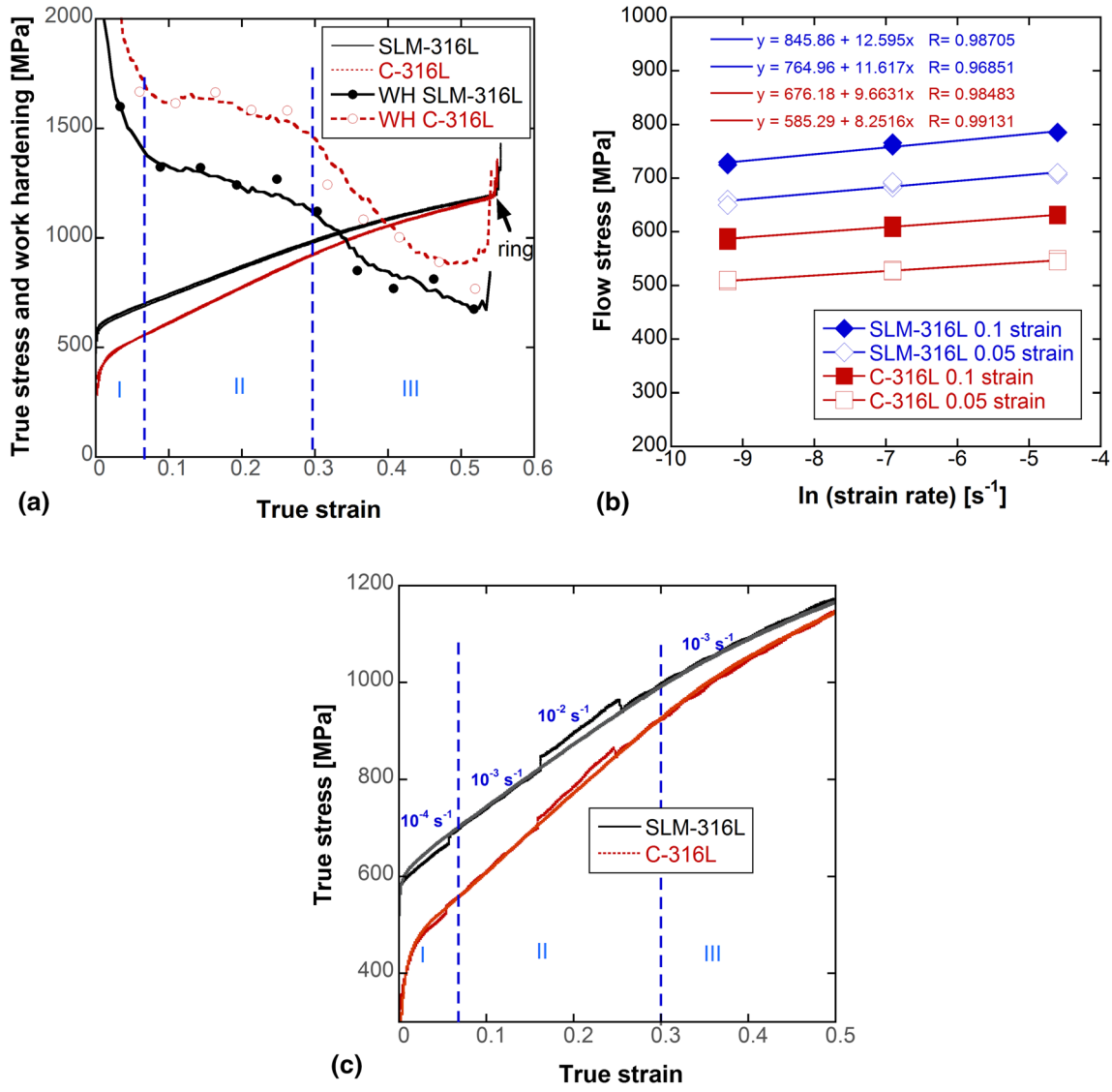

Fig. 3 (a) The compression true stress-strain (three samples) and typical work hardening-strain curves of SLM-316L and C-316L, (b) the flow stress versus ln strain rate at 0.05 and 0.1 strain, and (c) reloading stress-strain curves at quasi-static strain rates

dislocation density strengthening ($\Delta\sigma$) was determined to be 158 MPa based on Taylor's equation (Ref 34) given as

$$\Delta\sigma = M\alpha Gb\sqrt{\rho} \qquad \text{(Eq 3)}$$

where M is the Taylor's factor (2.9), b is the Burgers' vector (0.255 nm) α is an empirical constant (0.23), and G is the shear modulus (65 GPa) (Ref 35,36). This value of strengthening closely matches with the difference (150 MPa) in the yield strengths between the two alloys. However, the WH of C-316L is higher than that of SLM-316L until about large strains as seen in Fig. 3(a). The WH curves also distinguish three distinct deformation regions in Fig. 3(a): I-slip dominated, II- twinning and/or martensite transformation-induced slip deformation dominated, and III-reduced WH region. From the microscopic studies, which will be elaborated on later, SLM316-L is found to exhibit a twinning-dominated deformation, while C-316L is a martensite transformation-dominated deformation, both starting nearly at the same strain $\sim$ 0.07 and continue until about $\sim$ 0.3 strain (Fig. 3a). Figure 3(b) shows the variation of the flow stress at 0.10 and 0.05 strains with a logarithm of strain rate. The strain rate sensitivity parameters (β) of both alloys were determined based on the thermally activated deformation mechanism by the following relation (Ref 37).

$$\beta = \frac{\Delta\sigma}{\Delta\ln(\dot{\varepsilon})} \qquad \text{(Eq 4)}$$

where $\dot{\varepsilon}$ is the true strain rate. The slopes of the stress-ln (strain rate) curves are tabulated in Fig. 3(b) for each alloy at 0.05 and 0.1 strain. As is seen in the same figure, SLM-316L has a higher β-value at 0.05 and 0.1 strain within the quasi-static strain rates. The average values of the β parameter (average of 0.05 and 0.1 strain) are 12.1 and 8.9 MPa for SLM-316L and C-316L, respectively. Moreover, the β parameter increases with increasing strain. The strain rate jump tests shown in Fig. 3(c) further confirm the results of continuous loading stress-strain curves. An increase of strain rate from 1×10^{-4} to 1×10^{-3} s^{-1} in the region I increased the flow stress of SLM-316L by 20 MPa and C-316L by 15 MPa. In region II, when the strain rate is raised to 1×10^{-2} s^{-1}, the flow stress

increases to 30 and 20 MPa for SLM-316L and C-316L, respectively.

Figure 4(a) and (b) are the optical micrographs showing the twin regions (arrows) in SLM-316L tested at 0.11 and 0.51 strain, respectively. Twinning occurs locally and passes through the melt pool borders, as seen in the same figures. A more intense twin formation (smaller distance between twins) is also noted in the sample deformed at 0.51 strain. As with SLM-316L, the intensity of martensite plate formation in C-316L is noted to increase at increasing strains (0.11, 0.36, and 0.51), Figs. 4(c), (d), and (e). At the lowest strain (0.11), discrete martensite plates are seen in several grains (Fig. 4c), while few grains are fully filled with the plates at 0.36 strain (shown by the arrow in Fig. 4d). The martensite phase in the XRD spectrum of C-316L in Fig. 2 for the sample deformed until about 0.51 strain is determined about 45% by the Rietveld profile refinement method. As the strain increases, the calculated weight percentages of martensite increase almost linearly, as shown in Fig. 4(f).

The SEM micrographs were taken from the twin regions in Fig. 5(a), (b), (c), and (d) (indicated by the arrows) were further used to determine the distance between and thickness of twinned regions. The distance between twinned regions decreases from 6.5-8 μm with a thickness of $\sim$ 1 μm at 0.11 strain (Fig. 5a), to 3.5-4 μm with a thickness of $\sim$1.2 μm at 0.22 strain (Fig. 5b, to 1.5-2.5 μm with a thickness of $\sim$ 1 μm

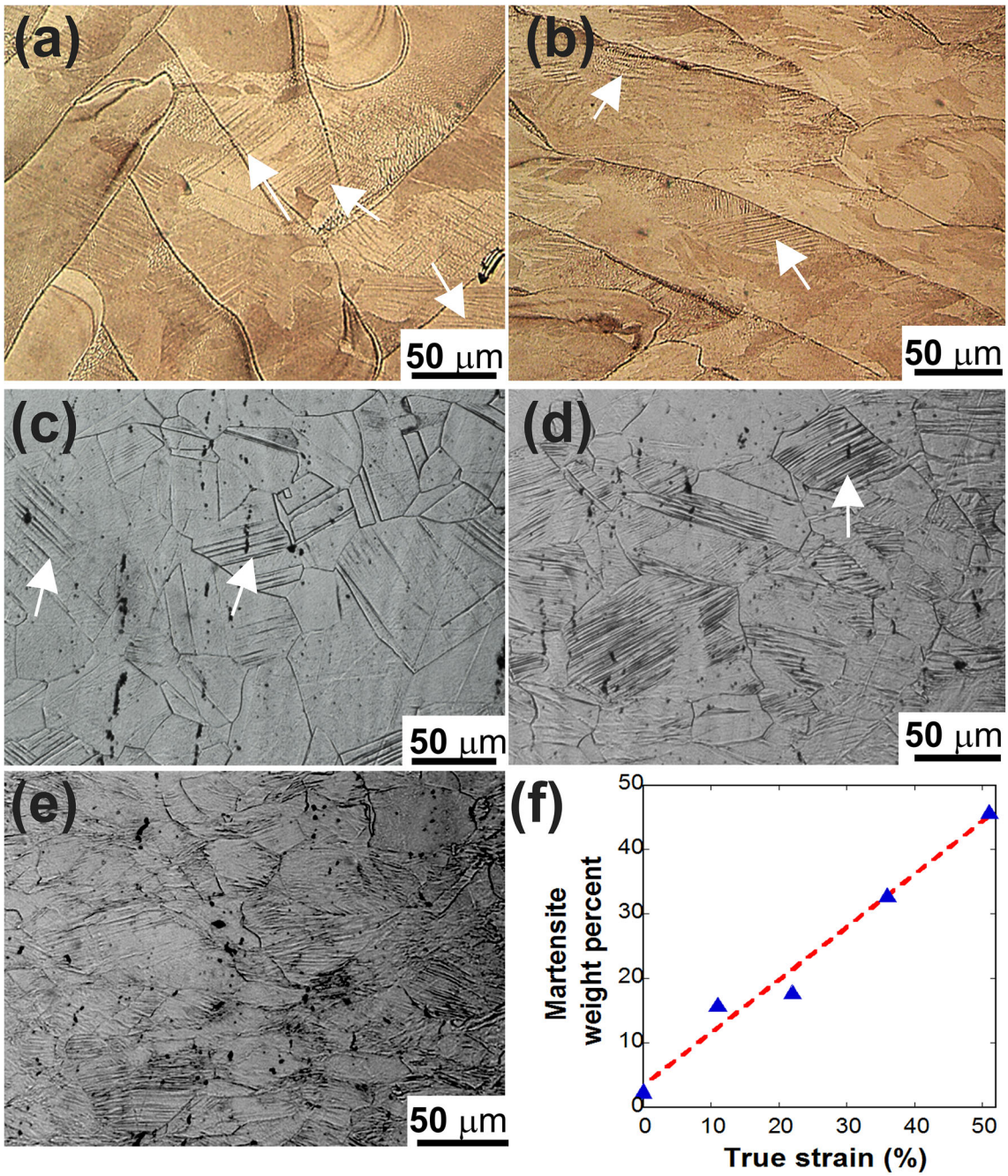

Fig. 4 The optical micrographs showing twinned regions in SLM-316L tested until (a) 0.11 and (b) 0.51 strain and martensite in C-316L tested until (c) 0.11, (d) 0.36 and (e) 0.51 strain, and (f) the martensite weight percent vs. true strain of deformed C-316L

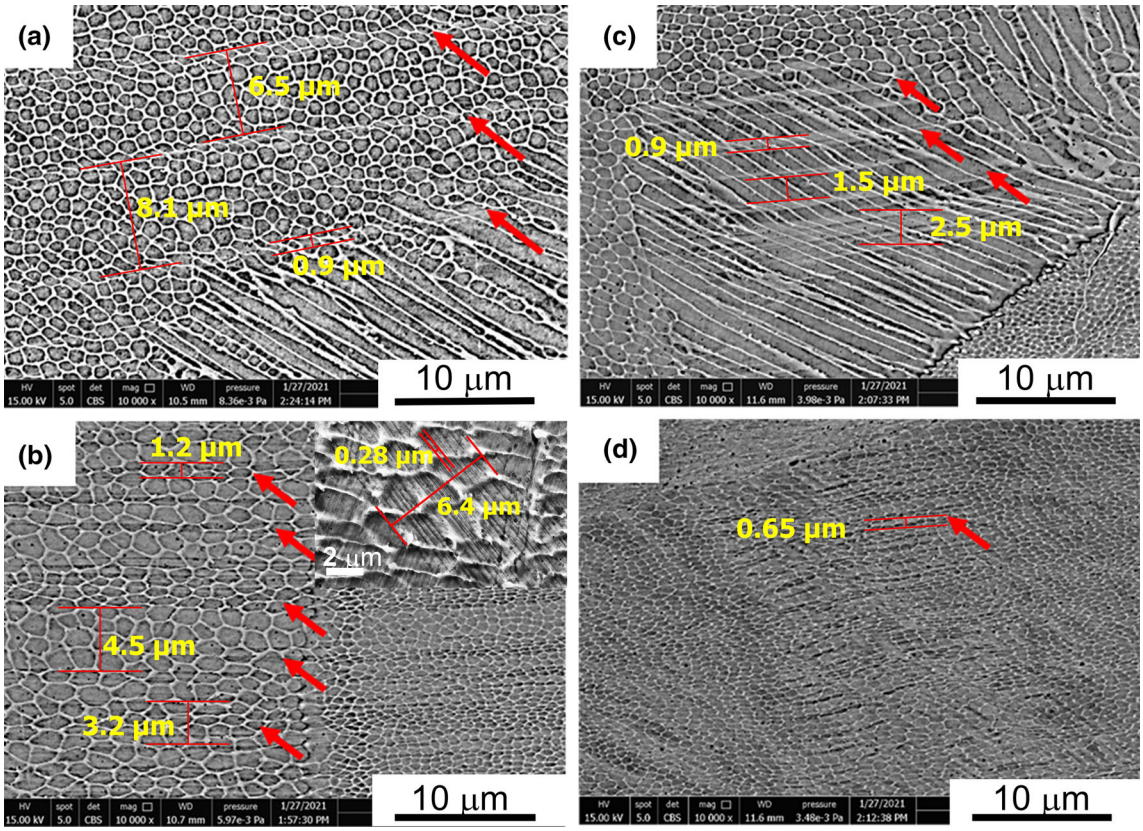

Fig. 5 The SEM micrographs showing twinned regions in SLM-316L deformed until about (a) 0.11, (b) 0.22, (c) 0.36, and (d) 0.51 strain

at 0.36 strain (Fig. 5c) and to less than 0.7 μm at 0.51 strain (Fig. 5d). As proposed previously (Ref 38), SLM-316L shows the twinning localized in certain regions on a very fine scale. The distance between twinned regions slightly decreases as the strain increases. The inset of Fig. 5(b) shows such a localized twinned region with a thickness of 6.4 μm. The distance between individual twins is in the order of 100 nm, which is less than the size of a sub-grain (0.7-1 μm). The fraction of twin regions also increases with increasing strain. Furthermore, the bent sub-grain seen in Fig. 5(c) in the twinned regions proves the twinning-activated deformation by the slip, resulting in the reorientation of slip planes.

Figure 6(a) shows a region of martensitic transformation near a grain boundary. The distance between martensite plates is about 1 μm with a thickness of $\sim$ 100 nm, as shown in the inset of Fig. 6(a). As noted in the same figure, a low fraction of twins is also seen (marked by arrows). The distance between these twins is $\sim$ 2 μm, but the thickness of the twinned region is comparably smaller than that in the SLM-316L sample. As the strain increases to 0.22, the fraction of the grains filled with martensite plates increases, while the distance between plates remains almost the same, 1 μm (Fig. 6b). Occasionally, twins are also seen at this strain, and the distance between them is $\sim$ 1 μm (Fig. 6b). The inset of Fig. 6(b) shows a deformation region in which twins are crossing a martensite plate. As the strain increases to 0.36, more martensite plates are formed, while the distance between martensite plates and twins remains almost constant around 1 μm (Fig. 6c). At the largest strain, 0.51, nearly all grains are filled with martensite plates, with a final distance of $\sim$ 0.7 μm between them (Fig. 6d). The thickness of and distance between twinned region and martensite plates are further tabulated as a function of deformation strain in Table 2.

The tested SLM-316L samples deform via twinning and slip similar to TWIP steels and C-316L martensitic transformation and slip similar to transformation-induced plastic deformation (TRIP) steels (Ref 39). A similar observation was made in a recent study on the tensile behavior of an SLM-316L and C-316L alloy (Ref 16). Increasing twin and martensite densities resulted in WH of SLM-316L and C-316L, respectively.

The strain rate sensitivity in the thermal activation-controlled deformation region will be inversely proportional to the activation volume (V^*) as (Ref 40).

$$V^* = \frac{MkT}{\beta} \qquad \text{(Eq 5)}$$

where k is the Boltzmann constant (1.38×10^{-23} J K^{-1}), and T is the absolute temperature. An increase in strain rate sensitivity of both alloys with increasing strain was therefore ascribed to the reduction of the deformation activation volume. Using the average β values, the activation volume is calculated as $59b^3$ and $80b^3$ for SLM-316L and C-316L, respectively. The activation volume for dislocation cross-slip is 10-100b^3. The formation of mechanical twinning and martensite was proposed to depend on the applied stress and the SFE (Ref 41). The typical range of SFEs for slip was reported as $>$ 45 mJ m^{-2}, for twinning 20-45 mJ m^{-2} and/or phase transformation $<$ 20 mJ m^{-2} for stainless steels (Ref 19). The low values of SFE induce a large separation between the Shockley partials, which prevents the cross-slip (Ref 37). Therefore, the cross-slip is not considered the rate-controlling in the investigated alloys.

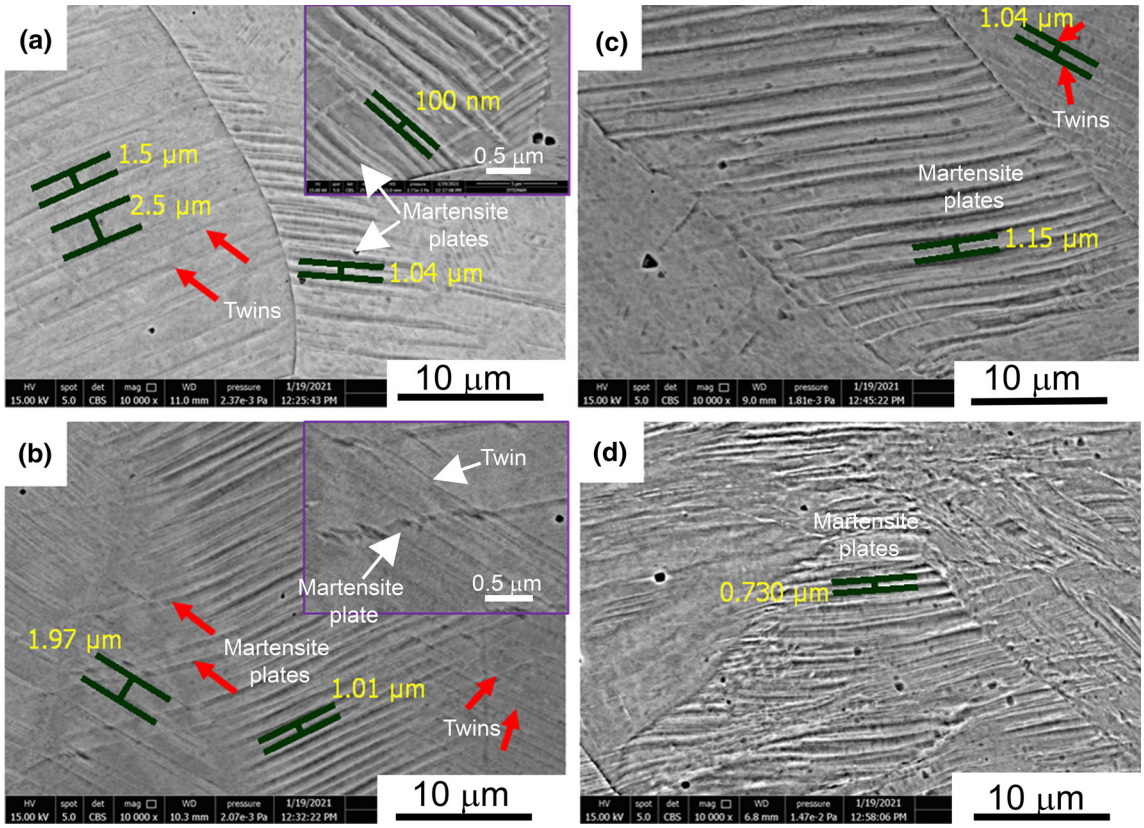

Fig. 6 The SEM micrographs showing martensite plates (also lesser number of twins) in C-316L deformed until about (a) 0.11, (b) 0.22, (c) 0.36, and (d) 0.51 strain

Table 2 The thickness of and distance between twinned region and martensite plates

Strain value	Thickness of twinned region, μm	Distance between twinned region, μm	Thickness of martensite plates, μm	Distance between martensite plates, μm
0.11	1	6.5-8	0.1	1
0.22	1.2	3.5-4	0.1	1
0.36	1	1.5-2.5	0.1	1
0.51		$<$ 0.7	0.1	0.7

A slight positive temperature dependency (Ref 42) or no temperature and strain rate dependency (Ref 43) were also reported for the twinning stress, and the martensitic transformation is a diffusion-less process (Ref 44). By also considering large grain sizes of both alloys, the deformation rate-controlling step in both alloys is determined as the dislocation emission from the twin and martensite boundaries (Ref 40). The higher strain rate sensitivity of SLM-316L is presumed to indicate a lower activation volume in the thermally activated deformation process than C-316L at the studies strain rate regime. This is in accordance with the measured distance between the observed twins in SLM-316L, in the level of 100 nm, and the distance between martensite plates, in the order of 1000 nm. Microscopically found twining that dominated deformation of SLM-316L may be due to the higher SFE of SLM-316L. The presence of N increases the SFE energy (Ref 45), promoting twinning rather than martensite transformation. As N_2 was used as a shielding gas in the fabricated SLM-316L samples, the N content may increase over that of C-316L. A 50 ppm higher N content was shown between 316L samples when the shielding gas changed from argon to nitrogen (Ref 46). This may be accounted for the detected difference in the deformation behavior of tested 316L alloys. However, a further detailed investigation is needed to verify the increased N content of SLM-316L and its effect on the SFE.

3.3 Hardness Tests

Figure 7(a) shows the variations of nano- and microhardnesses of SLM and C-316L samples with the depth of penetration (DOP). As seen in the same figure, the SLM-316L samples in the *yz*-plane show a higher hardness value than those in the *xy*-plane. The difference is likely due to the difference in the texture, grain morphologies, and sizes; the columnar grain widths in the *yz*-plane are several times smaller. As the DOP decreases to the sub-micron sizes, the difference in hardness values slightly decreases, but the difference still exists; although the sub-cell sizes are almost the same for both

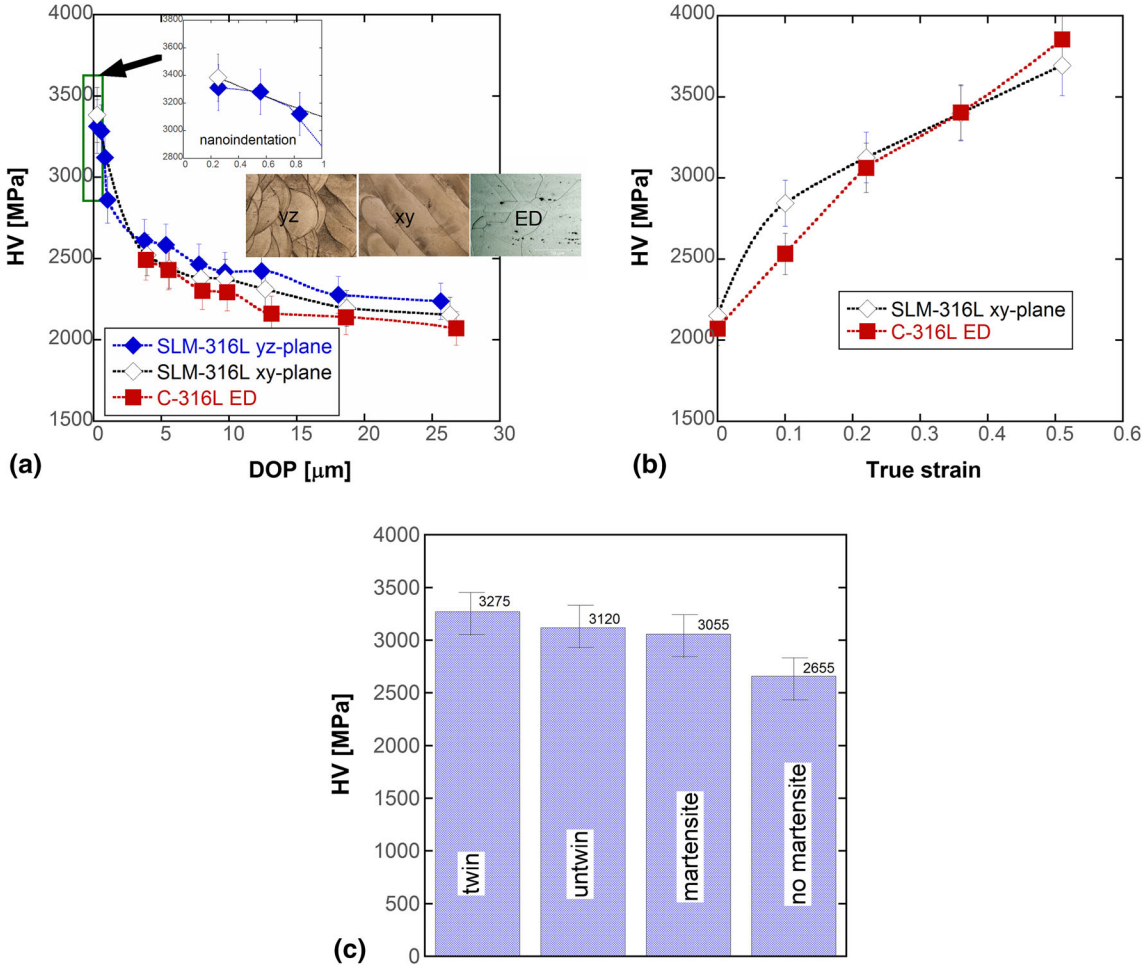

Fig. 7 (a) DOP vs. hardness, (b) the HV2 vs. true strain, and (c) HV0.5 of the regions of twin, untwin, and martensite and no martensite regions after 0.11 compression strain

planes. It was previously shown that these cells are in high dislocation density regions (dislocation networks) with higher solute atom concentrations such as Cr and Mo (Ref 20). The dislocation cell walls behaved as imperfect barriers to the dislocation motion (Ref 20,47). The lower yield strength of C-316L is also evident in Fig. 7(a). The response of C-316L to the reduced DOP is almost similar to that of SLM-316L, and the hardness increases as the DOP decreases. These results comply with the above assessment on the relatively low resistance of SLM-316L-cell walls to the dislocation motion. Figure 7(b) shows the variations in the hardness of the recovered SLM and C-316L samples after the prescribed compression strain. The higher WH of C-316L is also reflected in the same figure in which the hardness values of C-316L increase over those of SLM-316L after about 0.4 strains. To account for the effect of twinning and martensite on the strength, hardness tests were performed in the regions of the heavy twins and no twins in SLM-316L and heavy martensite and no martensite regions in C-316L after about 0.11 strain. A higher hardness increase in the martensite transformation is seen in Fig. 7(c), while the increase in hardness in twinning is moderate. Twin planes act as an obstacle to the dislocation motion and have an influence on the flow stresses similar to the grain size, Hall-Petch relation (Ref 41). As the deformation twins are continuously formed with increasing strain, the distance between twin planes decreases; hence, the distance taken by the dislocations, and this results in an increase in the flow stress. Both the presence of twin and martensite plates induce a more nonhomogeneous indentation as compared with the regions of no-twin and no-martensite, as seen in Fig. 8(a), (b), (c), and (d). The regions with twins and martensite (Fig. 8a, c) also show lesser numbers of slip lines as compared with the regions with no-twin and no-martensite (Fig. 8a, b). The higher WH of C-316L than SLM-316L is probably due to the higher resistance of the martensite plate than the twin boundary to the dislocation motion.

4. Conclusions

The deformation characteristics of an SLM-316L alloy were determined as compared with a C-316L alloy through compression tests until about the prescribed strain, and hardness tests were performed on the untested and compressed tested samples. Extensive microscopic observations showed that tested SLM-316L deformed dominantly by twinning and slip similar to TWIP steels, while C-316L by martensitic transformation and slip similar to TRIP steels. Within the studied quasi-static strain rate regime, SLM-316L showed higher flow stress and strain rate sensitivity but a lower WH than C-316L. The

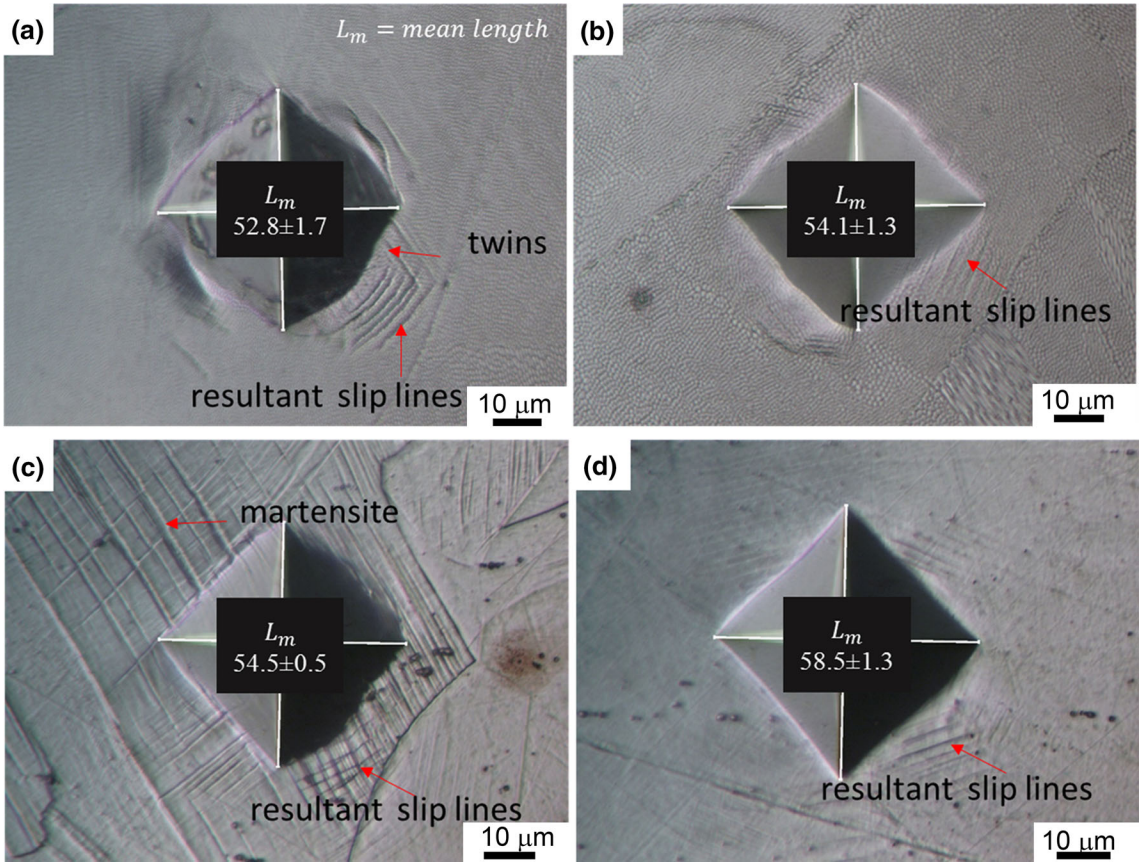

Fig. 8 The optical microscope of the indentations in the regions of (a) twin and (d) untwin in SLM-316L and (c) martensite and (b) no martensite in C-316L after 0.11 compression strain

higher strain rate sensitivity of SLM alloy was ascribed to the lower distances measured microscopically between nano-twins in the level of 100 nm in SLM-316L than the distance between martensite plates in the level of 1000 nm. A higher hardness increase in the martensite transformation region as compared with the twinned region proved the higher WH behavior of C-316L. The hardness tests in the micron and sub-micron level further confirmed the previously determined relatively low resistance of SLM-316L dislocation cell walls to the dislocation motion. The higher WH of C-316L than SLM-316L is probably due to the higher resistance of martensite plate than twin boundary to the dislocation motion.

Acknowledgments

The authors acknowledge financial support by the Scientific and Technological Research Council of Turkey within the support program 1515 for research and laboratory developments within Project Number 5189901. Moreover, the authors are grateful to the Materials Division of TUBITAK Marmara Research Center for providing the needed infrastructure.

References

1. I. Gibson, D. Rosen and B. Stucker, *Additive Manufacturing Technologies*, Springer, Berlin, 2014
2. B. Song, X. Zhao, S. Li, C. Han, Q. Wei, S. Wen, J. Liu and Y. Shi, Differences in Microstructure and Properties Between Selective Laser Melting and Traditional Manufacturing for Fabrication of Metal Parts: A Review, *Front. Mech. Eng.*, 2015, **10**(2), p 111–125
3. P. Mercelis and J.P. Kruth, Residual Stresses in Selective Laser Sintering and Selective Laser Melting, *Rapid Prototyp. J.*, 2006, **12**(5), p 254–265. (**in English**)
4. Z.C. Fang, Z.L. Wu, C.G. Huang and C.W. Wu, Review on Residual Stress in Selective Laser Melting Additive Manufacturing of Alloy Parts, *Opt. Laser Technol.*, 2020, **129**(15), p 106283. (**in English**)
5. T. Kim, K. Ha, Y.R. Cho, J.B. Jeon and W. Lee, Analysis of Residual Stress Evolution During Powder Bed Fusionprocess of AISI 316L Stainless Steel with Experiment and Numerical Modeling, *Int. J. Adv. Manuf. Technol.*, 2019, **105**(1–4), p 309–323. (**in English**)
6. H. Fayazfar, M. Salarian, A. Rogalsky, D. Sarker, P. Russo, V. Paserin and E. Toyserkani, A Critical Review of Powder-Based Additive Manufacturing of Ferrous Alloys: Process Parameters, Microstructure and Mechanical Properties, *Mater. Des.*, 2018, **144**, p 98–128. (**in English**)
7. P. Bajaj, A. Hariharan, A. Kini, P. Kurnsteiner, D. Raabe and E.A. Jagle, Steels in Additive Manufacturing: A Review of Their Microstructure and Properties, *Mater. Sci. Eng. A Struct. Mater. Prop. Microstruct. Process.*, 2020, **772**(25), p 138633. (**in English**)
8. J.J. Lewandowski and M. Seifi, Metal Additive Manufacturing: A Review of Mechanical Properties, *Annu. Rev. Mater. Res.*, 2016, **46**, p 151–186
9. K. Saeidi, X. Gao, Y. Zhong and Z.J. Shen, Hardened Austenite Steel with Columnar Sub-Grain Structure Formed by Laser Melting, *Mater. Sci. Eng. A Struct. Mater. Prop. Microstruct. Process.*, 2015, **625**, p 221–229. (**in English**)
10. Y. Zhong, L.F. Liu, S. Wikman, D.Q. Cui and Z.J. Shen, Intragranular Cellular Segregation Network Structure Strengthening 316L Stainless Steel Prepared by Selective Laser melting, *J. Nucl. Mater.*, 2016, **470**, p 170–178. (**in English**)
11. M. Zietala, T. Durejko, M. Polanski, I. Kunce, T. Plocinski, W. Zielinski, M. Lazinska, W. Stepniowski, T. Czujko, K.J. Kurzydlowski

and Z. Bojar, The Microstructure, Mechanical Properties and Corrosion Resistance of 316 L Stainless Steel Fabricated Using Laser Engineered Net Shaping, *Mater. Sci. Eng. A Struct. Mater. Prop. Microstruct. Process.*, 2016, **677**, p 1–10. (**in English**)
12. S. Gorsse, C. Hutchinson, M. Goune and R. Banerjee, Additive Manufacturing of Metals: A Brief Review of the Characteristic Microstructures and Properties of Steels, Ti-6Al-4V and High-Entropy Alloys, *Sci. Technol. Adv. Mater.*, 2017, **18**(1), p 584–610. (**in English**)
13. M.-S. Pham and P. Hooper, Roles of Microstructures on Deformation Response of 316 Stainless Steel Made by 3D Printing, *AIP Conf. Proc.*, 2017, **1896**(1), p 040017
14. M.S. Pham, B. Dovgyy and P.A. Hooper, Twinning Induced Plasticity in Austenitic Stainless Steel 316L made by Additive Manufacturing, *Mater. Sci. Eng. A Struct. Mater. Prop. Microstruct. Process.*, 2017, **704**, p 102–111. (**in English**)
15. Y.M. Wang, T. Voisin, J.T. McKeown, J. Ye, N.P. Calta, Z. Li, Z. Zeng, Y. Zhang, W. Chen, T.T. Roehling, R.T. Ott, M.K. Santala, P.J. Depond, M.J. Matthews, A.V. Hamza and T. Zhu, Additively Manufactured Hierarchical Stainless Steels with High Strength and Ductility, *Nat. Mater.*, 2017, **17**, p 63–71
16. Y.J. Yin, J.Q. Sun, J. Guo, X.F. Kan and D.C. Yang, Mechanism of High Yield Strength and Yield Ratio of 316 L Stainless Steel by Additive Manufacturing, *Mater. Sci. Eng. A-Struct. Mater. Prop. Microstruct. Process.*, 2019, **744**, p 773–777. (**in English**)
17. X.L. Wang, J.A. Muniz-Lerma, M.A. Shandiz, O. Sanchez-Mata and M. Brochu, Crystallographic-Orientation-Dependent Tensile Behaviours of Stainless Steel 316L Fabricated by Laser Powder Bed Fusion, *Mater. Sci. Eng. A Struct. Mater. Prop. Microstruct. Process.*, 2019, **766**(16), p 138395. (**in English**)
18. M.M. Ma, Z.M. Wang and X.Y. Zeng, A Comparison on Metallurgical Behaviors of 316L Stainless Steel by Selective Laser Melting and Laser Cladding Deposition, *Mater. Sci. Eng. A Struct. Mater. Prop. Microstruct. Process.*, 2017, **685**, p 265–273. (**in English**)
19. W. Woo, J.S. Jeong, D.K. Kim, C.M. Lee, S.H. Choi, J.Y. Suh, S.Y. Lee, S. Harjo and T. Kawasaki, Stacking Fault Energy Analyses of Additively Manufactured Stainless Steel 316L and CrCoNi Medium Entropy Alloy Using In Situ Neutron Diffraction, *Sci Rep*, 2020, **10**(1), p 1350. (**in English**)
20. L.F. Liu, Q.Q. Ding, Y. Zhong, J. Zou, J. Wu, Y.L. Chiu, J.X. Li, Z. Zhang, Q. Yu and Z.J. Shen, Dislocation Network in Additive Manufactured Steel Breaks Strength-Ductility Trade-Off, *Mater. Today*, 2018, **21**(4), p 354–361. (**in English**)
21. A. Rottger, K. Geenen, M. Windmann, F. Binner and W. Theisen, Comparison of Microstructure and Mechanical Properties of 316 L Austenitic Steel Processed by Selective Laser Melting with Hot-Isostatic Pressed and Cast Material, *Mater. Sci. Eng. A Struct. Mater. Prop. Microstruct. Process.*, 2016, **678**, p 365–376. (**in English**)
22. Z. Li, T. Voisin, J.T. McKeown, J.C. Ye, T. Braun, C. Kamath, W.E. King and Y.M. Wang, Tensile Properties, Strain Rate Sensitivity, and Activation Volume of Additively Manufactured 316L Stainless Steels, *Int. J. Plast.*, 2019, **120**, p 395–410. (**in English**)
23. T.J. Kneen, C. Barrett, G.P. Manogharan, P.R. Carlson, J. Dimon and B.P. Conner, Mechanical Behaviour and High Strain Rate Deformation of Stainless Steel 316L Processed by Selective Laser Melting, *Int. J. Rapid Manuf.*, 2020, **9**(9), p 84–102
24. W.C. Oliver and G.M. Pharr, An Improved Technique for Determining Hardness and Elastic Modulus Using Load and Displacement Sensing Indentation Experiments, *J. Mater. Res.*, 1992, **7**(6), p 1564–1583
25. W.C. Oliver and G.M. Pharr, Measurement of Hardness and Elastic Modulus by Instrumented Indentation: Advances in Understanding and Refinements to Methodology, *J. Mater. Res.*, 2004, **19**(1), p 3–20
26. D.L. Bish and S.A. Howard, Quantitative Phase Analysis Using the Rietveld Method, *J. Appl. Crystallogr.*, 1988, **21**(2), p 86–91
27. Z. Sun, X. Tan, S.B. Tor and C.K. Chua, Simultaneously Enhanced Strength and Ductility for 3D-Printed Stainless Steel 316L by Selective Laser Melting, *NPG Asia Mater.*, 2018, **10**(4), p 127–136
28. S.-H. Sun, T. Ishimoto, K. Hagihara, Y. Tsutsumi, T. Hanawa and T. Nakano, Excellent Mechanical and Corrosion Properties of Austenitic Stainless Steel with a Unique Crystallographic Lamellar Microstructure Via Selective Laser Melting, *Scr. Mater.*, 2019, **159**, p 89–93
29. T. Niendorf, S. Leuders, A. Riemer, F. Brenne, T. Tröster, H.A. Richard and D. Schwarze, Functionally Graded Alloys Obtained by Additive Manufacturing, *Adv. Eng. Mater.*, 2014, **16**(7), p 857–861
30. O. Andreau, I. Koutiri, P. Peyre, J.-D. Penot, N. Saintier, E. Pessard, T. De Terris, C. Dupuy and T. Baudin, Texture Control of 316L Parts by Modulation of the Melt Pool Morphology in Selective Laser Melting, *J. Mater. Process. Technol.*, 2019, **264**, p 21–31
31. T. Niendorf, S. Leuders, A. Riemer, H.A. Richard, T. Tröster and D. Schwarze, Highly Anisotropic Steel Processed by Selective Laser Melting, *Metall. Mater. Trans. B*, 2013, **44**(4), p 794–796
32. J.J. Marattukalam, D. Karlsson, V. Pacheco, P. Beran, U. Wiklund, U. Jansson, B. Hjorvarsson and M. Sahlberg, The Effect of Laser Scanning Strategies on Texture, Mechanical Properties, and Site-Specific Grain Orientation in Selective Laser Melted 316L SS, *Mater. Des.*, 2020, **193**(11), p 108852. (**in English**)
33. S. Morito, J. Nishikawa and T. Maki, Dislocation Density Within Lath Martensite in Fe-C and Fe-Ni Alloys, *ISIJ Int.*, 2003, **43**(9), p 1475–1477
34. G.I. Taylor, The Mechanism of Plastic Deformation of Crystals. Part I. Theoretical, *Proc. R. Soc. Lond. Ser. A Pap. Math. Phys. Charact.*, 1934, **145**(855), p 362–387
35. B.B. He, B. Hu, H.W. Yen, G.J. Cheng, Z.K. Wang, H.W. Luo and M.X. Huang, High Dislocation Density-Induced Large Ductility in Deformed and Partitioned Steels, *Science*, 2017, **357**(6355), p 1029–1032
36. T.S. Byun, On the Stress Dependence of Partial Dislocation Separation and Deformation Microstructure in Austenitic Stainless Steels, *Acta Mater.*, 2003, **51**(11), p 3063–3071
37. H. Conrad and H. Wiedersich, Activation Energy for Deformation of Metals at Low Temperatures, *Acta Metall.*, 1960, **8**(2), p 128–130
38. J.W. Christian and S. Mahajan, Deformation Twinning, *Prog. Mater. Sci.*, 1995, **39**(1–2), p 1–157
39. R.A. Hadfield, Some Newly Discovered Properties of Iron and Manganese, *Min. Proc. Inst. Civ. Eng.*, 1888, **93**(1888), p 61–75
40. Y.Z. Li and M.X. Huang, Carbon-Dislocation Interaction-Induced Abnormal Strain-Rate Sensitivity in Twinning-Induced Plasticity Steels, *Metall. Mater. Trans. A Phys. Metall. Mater. Sci.*, 2019, **50A**(6), p 2570–2575. (**in English**)
41. L. Rémy and A. Pineau, Twinning and Strain-Induced f.c.c. $\rightarrow$ h.c.p. Transformation on the Mechanical Properties of Co-Ni-Cr-Mo Alloys, *Mater. Sci. Eng.*, 1976, **26**(1), p 123–132
42. S. Mahajan and D.F. Williams, Deformation Twinning in Metals and Alloys, *Int. Metall. Rev.*, 1973, **18**(2), p 43–61
43. M.A. Meyers and K.K. Chawla, *Mechanical Behavior of Materials*, Cambridge University Press, Cambridge, 2009
44. M.A. Meyers, O. Vöhringer and V.A. Lubarda, The Onset of Twinning in Metals: A Constitutive Description, *Acta Mater.*, 2001, **49**(19), p 4025–4039
45. S. Lee, J. Kim, S.-J. Lee and B.C. De Cooman, Effect of Nitrogen on the Critical Strain for Dynamic Strain Aging in High-Manganese Twinning-Induced Plasticity Steel, *Scr. Mater.*, 2011, **65**(6), p 528–531
46. C. Pauzon, E. Hryha, P. Foret and L. Nyborg, Effect of Argon and Nitrogen Atmospheres on the Properties of Stainless Steel 316 L Parts Produced by Laser-Powder Bed Fusion, *Mater. Des.*, 2019, **179**(10), p 107873. (**in English**)
47. A.J. Birnbaum, H. Ryou, J.C. Steuben, A.P. Iliopoulos, K.J. Wahl and J.G. Michopoulos, Nested Size Effects in the Nanoindentation Response of Additively Manufactured 316L Stainless Steel, *Mater. Lett.*, 2020, **280**, p 128570